Surface mass transport and island nucleation during growth of Ge on laser textured Si(001)

T. Schwarz-Selinger
Centre for Interdisciplinary Plasma Science, Max-Plank-Institut für Plasmaphysik, EURATOM Association, D-85748 Garching, Germany and the Frederick Seitz Materials Research Laboratory, University of Illinois, Urbana, Illinois 61801

Y. L. Foo, David G. Cahill and J. E. Greene
Department of Material Science and Engineering and the Frederick Seitz Materials Research Laboratory, University of Illinois, Urbana, Illinois 61801

(Received 19 September 2001; published 12 March 2002)

Substrates with controlled surface morphologies are used to quantify the kinetics of surface mass transport during Stranski-Krastanov growth of epitaxial nanostructures. Morphologies are modified by laser texturing; tightly focused nanosecond laser pulses are used to produce micron-scale dimples on the surface of Si(001) substrates. The areal densities of three-dimensional Ge islands formed by chemical vapor deposition on these modified substrates is measured by atomic force microscopy for a wide range of Ge coverages (3–10 ML), temperatures ($500<T<700$ °C), and deposition rates ($0.003<F<0.3$ ML s^{-1}). Island nucleation is enhanced at the vicinal surfaces surrounding the rim of the laser dimples, and, as a consequence, a denuded zone with a reduced island density surrounds each dimple. The width of the denuded zone can be as large as 50 times the island spacing and is created by extensive mass transport during the formation of the wetting layer. Mass transport is driven by chemical-potential gradients associated with the wetting-layer thickness, substrate vicinality, and the elastic relaxation of three-dimensional islands. We find excellent agreement between the data and a one-dimensional model calculation of diffusion and nucleation; the fit to the model gives a transport rate of $Dn_0 \approx 1.5\times10^5\ s^{-1}$ at 600 °C and an activation energy $E_f+E_m \approx 1.3$ eV.

DOI: 10.1103/PhysRevB.65.125317 PACS number(s): 68.55.−a, 81.16.−c, 81.10.−h, 81.15.−z

I. INTRODUCTION

Deposition of Ge on clean Si(001) surfaces follows the Stranski-Krastanov (S-K) growth mode: three-dimensional (3D) islands form beyond a critical wetting layer thickness of ≈four equivalent monolayers (eq ML) [1 eq ML Si(001) $=6.78\times10^{14}$ cm^{-2}]. The driving force for island formation is the misfit strain caused by a 4.2% difference in the lattice constants of Ge and Si. At the cost of increased surface energy, 3D islands reduce strain energy by elastic deformation of the island and substrate. Beginning with the realization more than ten years ago[1] that islands formed in S-K growth can be coherent with the substrate, S-K growth has been under intense investigation because of fundamental interest in this method of synthesizing epitaxial nanostructures and excitement over possible applications in microelectronics.

Future applications may demand a narrow distribution of island sizes and a regular arrangement of the islands on the surface; therefore, many studies have examined the mechanisms that control the island size, size distribution,[2,3] areal density,[4] and in-plane ordering. Even in the simplest case of homogeneous nucleation on unpatterned substrates, the spectrum of thermodynamic and kinetic factors that controls islanding is exceedingly complex and probably system specific. For example, in the Ge/Si(001) system, nucleation barriers produced by surface energy anisotropy inhibit the continuous evolution of island shapes and produce the striking bimodal size distribution of so-called ''pyramid''- and ''dome''-shaped islands.[2,3,5,6] Heterogeneous nucleation on substrates patterned by lithography or by naturally occurring growth processes adds even greater complexity.[7–13]

Although mass transport on the surface of the wetting layer underlies most of the other detailed mechanisms of island nucleation, shape transitions, and subsequent coarsening in S-K growth, quantitative measurements of the kinetics present many difficulties. Traditional methods of measuring surface mass transport using the decay of periodic morphologies are not applicable because the wetting layer is only a few monolayers thick. Low-energy electron microscopy (LEEM) is a powerful method for measuring step mobilities but the step density on the wetting layer is high and individual steps cannot be resolved in a typical LEEM experiment. In homoepitaxial growth and heteroepitaxy without a wetting layer (the Volmer-Weber growth mode), kinetics of surface transport can sometimes be deduced from measurements of island densities[14] but the validity of this approach for analyzing S-K growth is unclear: thermal fluctuations of the thickness of the wetting layer are possibly more important in determining nucleation rates than the supersaturation of adatom density created by the growth flux.

The difficulty of using island densities for deducing mass transport is further illustrated in Fig. 1 where we plot our data for Ge(001)/Si growth at a fixed coverage of 7 eq ML as a function of growth rate and temperature. Clearly, the island densities do not show the smooth dependence on temperature and flux predicted by rate equation models or classical nucleation theory; a large critical nucleus can be expected based on the relatively small formation energy of surface ad-dimers[15] and, therefore, the island density should increase linearly with the growth rate. Transitions in island shapes are probably at least partially responsible for the complicated behavior shown in Fig. 1. At 500 °C, rectangular huts initially dominate and then transform into more stable square-based pyramids with increasing Ge coverage. At 550 °C, the

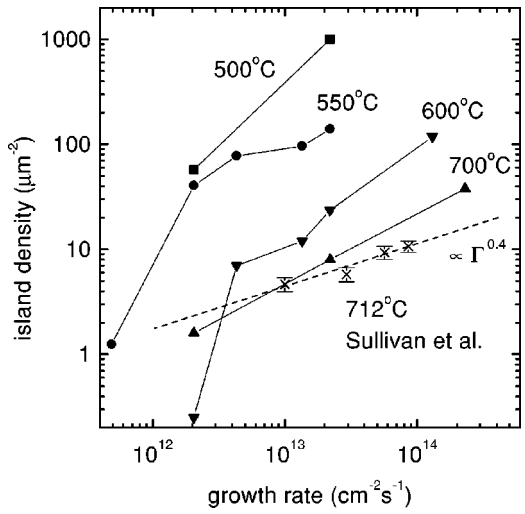

FIG. 1. Sum of dome and pyramid island densities as a function of growth rate and substrate temperature: 500 °C (squares), 550 °C (circles), 600 °C (down triangles), and 700 °C (up triangles). The total Ge coverage is fixed at ≈7 eq ML. Data of Sullivan *et al.*, Ref. 4, for growth at 712 °C (crosses) by low-pressure chemical vapor deposition are included for comparison together with their power-law fit for the flux Γ dependence of the island density.

island distribution is bimodal consisting of pyramids and faceted domes and at 600 °C, multifaceted domes dominate the distribution except for higher growth rates, where pyramids are also present. Furthermore, intermixing of the deposited Ge with the Si substrate[16–18] becomes important at higher temperature and the lowest growth rates.

The terms ''diffusion length,'' ''diffusivity,'' and ''migration length'' are commonly used in discussions of surface kinetics but the definitions of these terms are often unclear. In this work, we use ''diffusivity'' D to describe the random walk of the surface defect that dominates the mass transport. For the Ge(001) surface, this surface defect is likely to be the ad-dimer. The rms displacement of the ad-dimer during its lifetime τ as a surface defect is the migration length $l_m = \sqrt{4D\tau}$. We define the diffusion length L_d as the distance over which the wetting-layer thickness can respond to gradients in the surface chemical potential during an experimental time scale Δt. As we discuss in more detail below, $L_d = \sqrt{4\sigma D n_0 \Delta t}$, where n_0 is the equilibrium density of ad-dimers, and σ is the area of a dimer. Because the product Dn_0 has units of inverse time, we refer to this fundamental property of the surface as the ''transport rate.''

Previous discussions of wetting-layer mass transport[19,20,13,4] have reached widely varying conclusions on the values of l_m or L_d. To gain insight, we modify the morphology of Si(001) substrates using laser texturing; these changes in surface morphology drive mass transport during the formation of the wetting layer. Thinning of the wetting layer is revealed by a denuded zone in the island density surrounding the laser dimples. Using a simple one-dimensional model of diffusion and nucleation, we analyze measurements of the width of the denuded zone as a function of flux and temperature and thereby quantify the transport rate Dn_0.

II. EXPERIMENTAL DETAILS

We use *p*-type Si(001) substrates with a resistivity of 1 Ω cm. Our process for modifying the substrate morphology by laser texturing[21] uses single pulses of a passively *Q*-switched and frequency doubled (532 nm) neodymium yttrium aluminum garnet laser. We create relatively small and deep laser dimples by tightly focusing the laser pulse to a $1/e^2$ diameter of ≈2.6 μm with a peak energy density of ≈1.1 J cm^{-2}. Laser dimples form because radial temperature gradients in the melt zone produce surface-tension gradients that drive fluid away from the center of the melt.[21] Subsequent inspection by plan-view transmission electron micrography shows that the laser dimples are free of dislocations and planar defects. Texturing is done in air prior to cleaning and loading the substrates into the deposition chamber.

The textured substrates are degreased by successive rinses in organic solvents and four wet chemical oxidation/etch cycles. The substrates are then dried and exposed to UV radiation from a low-pressure Hg lamp to form an SiO_2 passivation layer. Immediately prior to loading the substrates into the deposition chamber, they are etched again for 30 sec in dilute (1%) HF, dried, and exposed to UV radiation for 30 min. Cleaning within the vacuum chambers consists of degassing the substrate and holder for 4 h at 600 °C and removal of the oxide by several rapid temperature excursions to 1150 °C for a few seconds with a heating rate of 100 °C s^{-1}. During the high-temperature flashes, the dimple shape changes because of rapid step motion.[22] Although our experimental results are only weakly dependent on the dimple shape, the flashing procedure is identical for each sample.

We use gas-source molecular beam epitaxy to deposit Si and Ge on the laser textured surfaces; our ultrahigh-vacuum deposition and analysis system is described in detail in Ref. 23. Precursor gases are delivered through individual tubular dosers located 3 cm from the substrate at an angle of 45°. Digermane and disiliane precursors traverse the small distance from the doser to the sample ballistically; hence, the terminology ''gas-source molecular beam epitaxy'' is often used to describe this growth process. We heat the sample by dc current and calibrate the substrate temperature as a function of the heating current using a test substrate equipped with a bonded thermocouple. The temperature calibration was cross checked with two infrared pyrometers. By accurately cutting the samples to a standard width, we are able to achieve good reproducibility of the substrate temperature, ±5 °C.

Each experiment begins with the growth of a Si buffer layer at a substrate temperature of 800 °C from a undiluted disilane flux of 2.2×10^{16} cm^{-2} s^{-1}. The growth time is 30 sec, resulting in a 11 nm thick buffer layer.[24] After the disilane source is turned off, the substrate temperature is held at 800 °C for 45 sec, rapidly lowered to the growth temperature (100 °C s^{-1}), and held for 15 sec before the digermane flux (14.2 vol % Ge_2H_6 in He) is initiated. Immediately after Ge deposition at $500<T<700$ °C, the sample heater is turned off and the sample cools rapidly to $T<200$ °C.

Since the Ge growth temperatures are well above the

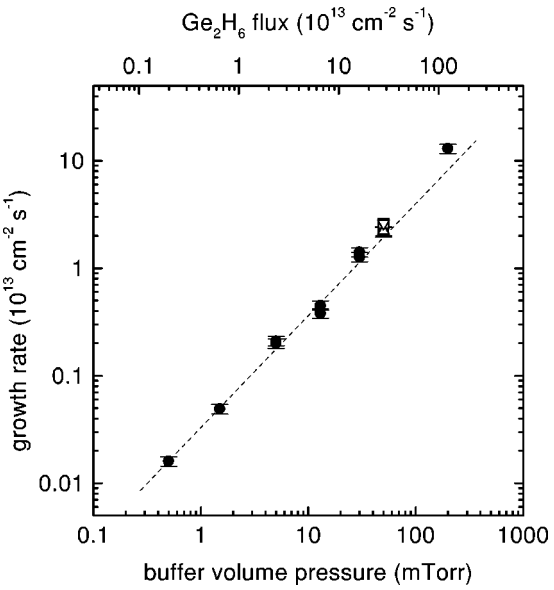

FIG. 2. Average Ge growth rate (Ge coverage measured by Rutherford backscattering spectroscopy divided by deposition time) after deposition of ≈ 7 eq ML of Ge as a function of buffer volume pressure for substrate temperature of 600 °C (filled circles). The dashed line fit is the linear dependence expected for a constant sticking coefficient. Data for 500 °C (open square), 550 °C (open up triangle), and 700 °C (open down triangle) are shown for a buffer volume pressure of 50 mTorr; all four data points at 50 mTorr overlap, demonstrating that the growth rate is also independent of temperature for $500 < T < 700$ °C. The scale of the top axis is approximate.

monohydride desorption temperatures, 290°–340 °C for Ge(001),[25,26] the deposition rate should increase linearly with the digermane flux. To verify this assumption, we grew a set of samples at a substrate temperature of 600 °C and varied the digermane flux by changing the pressure p of the constant-pressure reservoir, 0.5 mTorr $< p <$ 200 mTorr, corresponding to a digermane flux Γ of 2×10^{12} cm^{-2} s^{-1} $< \Gamma < 10^{15}$ cm^{-2} s^{-1}. In addition, we examined the temperature dependence of the growth rate at fixed flux. Figure 2 shows the average growth rate as a function of reservoir pressure for these two sets of experiments. Over the entire range of our growth parameters, the average digermane sticking coefficient is constant, $S \approx 0.05$, in agreement with a previous analysis of SiGe growth kinetics.[24] Similar experiments for the coverage versus deposition time (data not shown) reveal that the sticking coefficient during growth of the first monolayer is significantly larger than for subsequent monolayers. The sticking coefficient of digermane on clean Si(001) was previously determined[24] to be $S \approx 0.28$.

Island distributions are analyzed with atomic force microscopy (AFM) in tapping mode. AFM provides accurate island height and densities but—because of the finite size and the unknown shape of the probe tip—measurements of island diameters are often unreliable. We therefore supplement the AFM data with scanning electron microscopy (SEM). In agreement with the work of Kamins *et al.*,[19] we find that the diameters of dome-shaped islands measured by AFM appear ~ 30 nm larger than the measured by SEM.

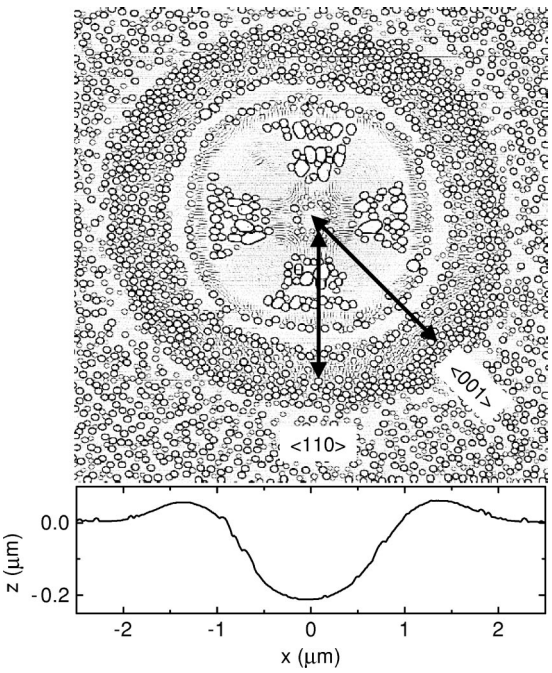

FIG. 3. High-pass filtered AFM image of a 260 nm deep laser dimple after deposition of 6.8 eq ML of Ge at 600 °C and a growth rate of 11.4 eq ML min^{-1}. The area of the image is 5×5 μm^2. The plot at the bottom of the figure shows a line scan of the surface height through the center of the dimple.

Areal atomic densities of Ge are measured by Rutherford backscattering spectroscopy (RBS) using 2 MeV He^+ ions incident at 22.5 ° to the sample normal and a scattering angle of 150°. Backscattering spectra are analyzed using SIMNRA software[27] and stopping-power data of Ziegler.[28]

III. EXPERIMENTAL RESULTS

A. Nucleation on vicinal surfaces

Figure 3 shows a typical 5×5 μm^2 AFM image of a laser dimple after deposition of 6.8 eq ML of Ge at 600 °C and a growth rate of 11.4 eq ML min^{-1}. The image is highpass-filtered to visualize the locations of islands on the curved surfaces of the laser dimple. A bimodal size distribution forms at this high growth rate: 40 nm wide square-based pyramids coexist with 70 nm diameter domes. Far from the dimple, the island densities are uniform, 70 μm^{-2} for domes and 50 μm^{-2} for pyramids.

The morphology of the laser dimple alters the island distribution in several ways: (i) the island density on the outer rim of the dimple is greatly enhanced compared to the unmodified surface, (ii) island nucleation is suppressed on the (001) oriented regions at the bottom of the dimple and along the top of the rim, (iii) large dislocated islands form inside the rim of the dimple along the $\langle 110 \rangle$ directions, and (iv) inside the rim along the $\langle 001 \rangle$ directions, nucleation is suppressed. Although the island density is enhanced on the outer rim of the laser dimple, the island size distribution on the rim is the same as the distribution on the unmodified surface.

Growth experiments at lower Ge coverages (data not shown) reveal that islanding occurs first on the inside of the

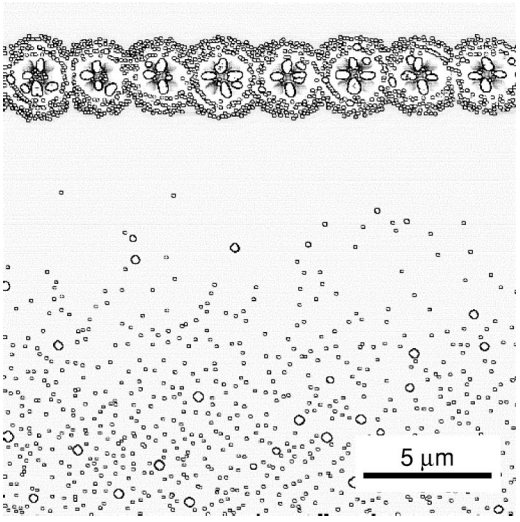

FIG. 4. Highpass-filtered AFM image, 20×20 μm^2, of a row of 270 nm deep laser dimples after a Ge coverage of 7 eq ML, deposited at 600 °C and a growth rate of 0.4 ML min^{-1}. The denuded zone in the island density is several microns wide.

dimple; the initial nucleation sites are vicinal surfaces tilted by $12°\pm2°$ with respect to the (001) orientation of the substrate. At higher coverages, large dislocated islands often appear at these sites, e.g., the four ⟨110⟩ oriented regions in the center of the dimple in Fig. 3.

B. Denuded zone

When Ge is deposited at high rates, see Fig. 3, the island density on the unmodified surface is reduced in only a narrow region surrounding the rim of the dimple. At low growth rates, this denuded zone expands dramatically, see Fig. 4. To improve counting statistics for the island densities, we arrange the laser dimples in a row. For the example shown in Fig. 4, the ≈4 μm diameter dimples are aligned along a ⟨110⟩ direction with a center-to-center spacing of 2.75 μm. The growth rate for this surface, 0.4 ML min^{-1}, is ≈25 times smaller than for the surface shown in Fig. 3.

We again observe enhanced nucleation on the outer rim of the dimples and large dislocated islands inside the dimples. The island distribution on the unmodified surface is dominated by multifaceted domes with a narrow range of sizes; the average dome is 67 nm in diameter and 17 nm tall. No pyramids are observed at this growth rate and coverage. A small number of dislocated islands also appear on the unmodified surface; the areal density of these so-called ''superdomes'' is 0.2 μm^{-2}. But the most dramatic difference between the morphologies shown in Figs. 3 and 4 is the large denuded zone on the unmodified surface adjacent to the row of dimples. Only a few islands have nucleated within 4 μm of the laser dimples and suppression of the island density extends to 12 μm from the dimple edges.

All of the data reported in this work were collected on samples with laser dimples that are ≈260 nm deep but we also examined how the denuded zone varies with the dimple depth. For depths between 100 and 300 nm, the experimental results are independent of the dimple depth. For shallower

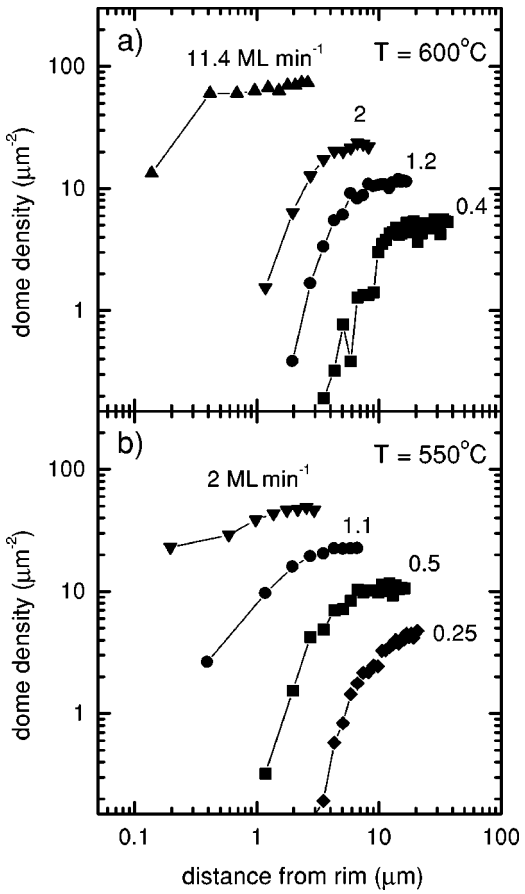

FIG. 5. Densities of dome-shaped islands as a function of lateral distance from the outer rim of the laser dimples for different growth rates. (a) Growth temperature $T=600$ °C; (b) $T=550$ °C. Each curve is labeled by the Ge growth rate in equivalent monolayers per minute.

dimples, the island density does not drop completely to zero near the dimple but the overall extent of the region with a suppressed island density remains constant. But even for dimples only ≈3 nm deep, a region of suppressed island density is still visible.

In Fig. 5 we summarize measurements of the local island density in the vicinity of the laser dimples for several growth rates and two growth temperatures. The Ge coverage for each of these eight experiments is between 6 and 7 eq ML. We concentrate on the density of dome-shaped islands to make the comparisons more quantitative; the relative variations in the densities of pyramids are similar but the domes are more accurately resolved in the AFM images. Island densities in regions far from the laser dimples increase monotonically with growth rate, see also Fig. 1. Increasing the growth rate shrinks the overall extent of the denuded zone and the width of the region where the island density is completely suppressed.

To further probe the mechanisms responsible for the denuded zone, we examine changes in the denuded zone created by postgrowth annealing. In these experiments, we deposit Ge at 600 °C using a growth rate of 2 eq ML min^{-1}. After 3 min of growth (6 eq ML), we anneal the samples in the deposition chamber at 600 °C for between 0 and 30 min

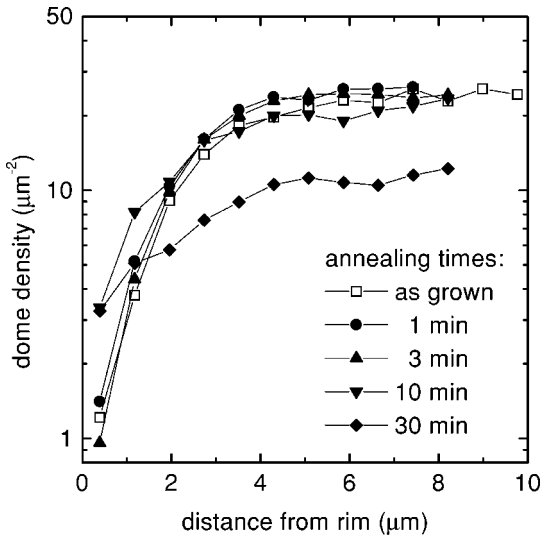

FIG. 6. Density of dome-shaped islands as a function of lateral distance from the outer rim of the laser dimples for four different annealing times at 600 °C. The growth parameters are $T=600$ °C, growth rate 2 eq ML min^{-1}, and coverage 6 eq ML. Although ripening is significant during a 30 min anneal, the extent of the denuded zone is unchanged.

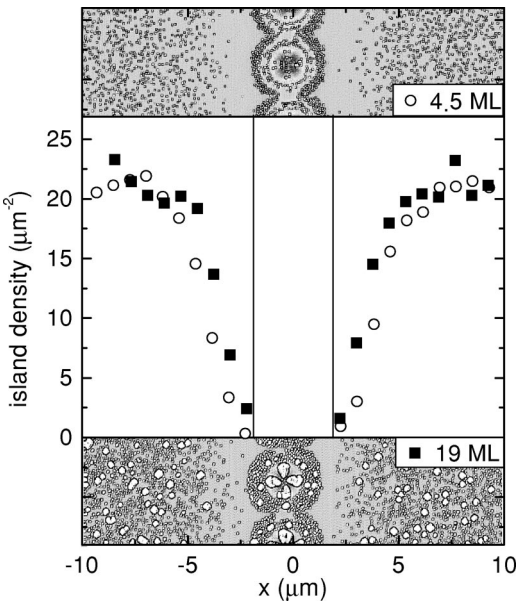

FIG. 7. Island distribution as a function of position for 2 min (open circles, 4.5 eq ML Ge) and 10 min (solid squares, 19 eq ML Ge) growths at $T=600$ °C. The top and bottom of the figure include sections of the corresponding AFM images that were used to calculate the island densities. The images are highpass-filtered.

and analyze the island densities as before, see Fig. 6. Samples annealed for one and three minutes are identical to the as-grown sample within the accuracy of the measurement. The sample annealed for 10 min shows a slightly smaller island density far from the dimple and an increase in the island density close to the dimple. With a 30 min anneal, ten times the growth time, the island density far from the dimple decreases by a factor of 2 but the overall extent of the denuded zone remains ≈ 5 μm.

On the surface of the sample annealed for 30 min, dome-shaped islands coexist with a broad size distribution of pyramids. Ring-shaped depressions, <1 nm deep, are also observed. Some of these rings surround a single small pyramid. Because the diameter of the rings is equal to the diameter of the initial dome-shaped islands—and because the sum of the areal densities of rings and the remaining domes is the same as the dome density of the as-grown sample—we conclude that the rings are the remnants of domes that have disappeared during the ripening process.[2]

Finally, we discuss samples prepared with different Ge coverages to study the denuded zone at different stages of growth. At 600 °C and a growth rate of 2 eq ML min^{-1}, samples were grown for 2, 3, 4, and 10 min. Although the islands size distribution evolves from a mixture of pyramids and domes (2 min) to pure domes (3 min) and then to a mixture of domes and a small number of superdomes (4 min), the extent of the denuded zone is the same in all three cases. Only for the highest Ge coverage can we detect a small change in the characteristics of the denuded zone, see Fig. 7. At a coverage of 19 eq ML, 10% of islands are dislocated superdomes with an average height and diameter of 50 and 200 nm, respectively. The superdomes show the same decrease in island densities as the domes. The data in Fig. 7 demonstrate that the denuded zone narrows by only a small amount when the coverage is changed by a factor of ≈ 5.

IV. ONE-DIMENSIONAL MODEL OF DIFFUSION AND NUCLEATION

We developed a one-dimensional model of mass transport and island nucleation to model the width of the denuded zone as a function of deposition rate, temperature, and coverage. We assume that the deposition flux produces only a small perturbation on the areal density of surface defects, presumably ad-dimers, responsible for mass transport on the surface of the wetting layer.[15] Therefore, the areal density n of Ge ad-dimers follows the diffusion equation

$$D\nabla^2 n = \frac{1}{\Omega}\frac{\partial h}{\partial t} - F, \tag{1}$$

where D is the diffusivity of an ad-dimer, Ω is the volume of the ad-dimer, h is the wetting-layer thickness, and F is the formation rate of ad-dimers created by the deposition flux.

This partial differential equation for n and h is coupled to an algebraic expression relating n and h because we assume that the local density of ad-dimers n is controlled by local differences in the chemical potential $\Delta\mu$ of the wetting layer. Tersoff[29] used empirical potentials to calculate the surface energy per atom for Ge wetting layers as a function of thickness. Daruka and Barabási[30] suggest an approximate exponential form for the change in the chemical potential with thickness

$$\Delta\mu = -\phi \exp(-h/h_0), \tag{2}$$

where ϕ and h_0 are parameters that describe the wetting forces[29,30] between Ge and Si that decay with wetting-layer thickness. By fitting Tersoff's results[29] (plotted as square symbols in Fig. 3 of Ref. 29), we estimate $\phi = 0.1$ eV and $h_0 = a$ where a is the thickness of one Ge layer for the ad-dimer. We multiply Tersoff's calculation by a factor of 2 to make our $\Delta\mu$ appropriate for ad-dimers.

The local density of ad-dimers n is

$$n = n_0 \exp[\Delta\mu/(k_B T)], \tag{3}$$

where n_0 is the ad-dimer density of a thick and coherent wetting layer. We then rewrite Eq. (1) in dimensionless form,

$$\sigma\nabla^2 \exp\left(\frac{\Delta\mu}{k_B T}\right) = \frac{\partial(h/a)}{\partial(tDn_0)} - \frac{\sigma F}{Dn_0}, \tag{4}$$

and note that the evolution of the wetting-layer thickness h is a function of the transport rate Dn_0 and not D or n_0 independently; σ is the area per ad-dimer, $\sigma = \Omega/a$.

Nucleation is treated in our model by assuming that each surface site has a nucleation rate r that depends only on the local thickness of the wetting layer h. By analogy with classical nucleation theory of crystallization of an undercooled melt,

$$r = r_0 \exp[-\xi/(h - h_c)], \tag{5}$$

where r_0 and ξ are parameters that we vary to give island separations in agreement with experiment, and h_c is the critical wetting-layer thickness for the formation of three-dimensional islands; experiments[31,32] suggest $h_c \approx 4a$. When an island nucleates, we create a new boundary condition on Eq. (4) that maintains the wetting-layer thickness at $h_i = 3a$ in the vicinity of the island. Thus, since $h_i < h_c$, an island suppresses further nucleation in its immediate neighborhood. This value for h_i is suggested by analysis of the mass balance between wetting layer and islands in annealing experiments.[2] Although we have not extensively explored the behavior of this nucleation model as a function of the parameters, the island density per unit length is mostly controlled by $\sqrt{F/(Dn_0)}$ and is remarkably insensitive to the choices of r_0, ξ, and h_i. We find that when Dn_0 is adjusted to fit the experimental measurements of the widths of the denuded zones, the island densities are fit by $\xi = 2a$ and $r_0 = 100\ \mathrm{s}^{-1}$.

Finally, we must incorporate the properties of the rim of the laser dimples. In our first attempts, we modeled the rim of the laser dimple by creating a region in the center of our one-dimensional simulation cell with a lower value of h_c in Eq. (5); this method of forcing early nucleation creates a denuded zone but gives poor agreement with the flux dependence of the data. Instead, we found that adding a second term to Eq. (2) gave much better agreement with experiment. We create a Gaussian-shaped region at the center of our one-dimensional simulation cell with a lowered chemical potential,

$$\Delta\mu = -\phi \exp(-h/h_0) - \chi \exp[-(x/x_0)^2]. \tag{6}$$

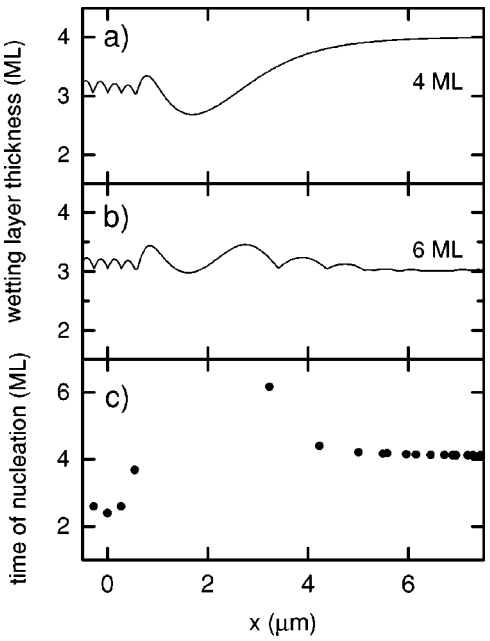

FIG. 8. Output from the 1D model of Sec. IV for growth at 600 °C and $F = 1.2$ ML min^{-1}; (a) wetting-layer thickness h after deposition of 4 eq ML; (b) wetting-layer thickness after deposition of 6 eq ML; (c) time at which each that island nucleates measured in units of the time required to deposit 1 eq ML. The minimum in the chemical potential of the substrate is at $x = 0$, see Eq. (6).

We are unaware of any estimates of how the chemical potential of the wetting layer varies with substrate orientation but, fortunately, the simulation is relatively insensitive to our choice of χ and we fix $\chi = \phi = 0.1$ eV. The simulation *is* sensitive to x_0: while a more rigorous calculation might succeed in relating x_0 to the geometry of the rim of the laser dimple, we currently treat x_0 as a free parameter. We expect, however, that $2x_0$ should be comparable to the distance from the top of the rim of the laser dimple to the outer edge of the laser dimple, ~ 1 μm, see Fig. 3. The simulation proceeds by numerically integrating the diffusion equation, Eq. (4), randomly creating islands using Eq. (5), maintaining the boundary condition $h = h_i$ near islands, and updating the chemical potential $\Delta\mu$ according to Eq. (6).

To constrain the temperature dependence of the transport rate Dn_0, we assume that Dn_0 is thermally activated with an activation energy equal to the sum of the ad-dimer formation and migration energies, $E_m + E_f$:

$$Dn_0 = \nu \exp\left(-\frac{E_m + E_f}{k_B T}\right), \tag{7}$$

where ν is a microscopic attempt frequency that we fix at 5×10^{12} s^{-1}. We fit the eight experimental results shown in Fig. 5 by varying the two important parameters $(E_m + E_f)$ and x_0 and find $E_m + E_f = 1.3$ eV and $x_0 = 800$ nm.

An example of the output of the calculation is shown in Fig. 8 for growth at 600 °C and a growth rate of 1.2 ML min^{-1}. Figure 8(a) shows the wetting-layer thickness after 200 s of growth; i.e., a deposition of 4 eq ML. Because of diffusion driven by the chemical-potential gradi-

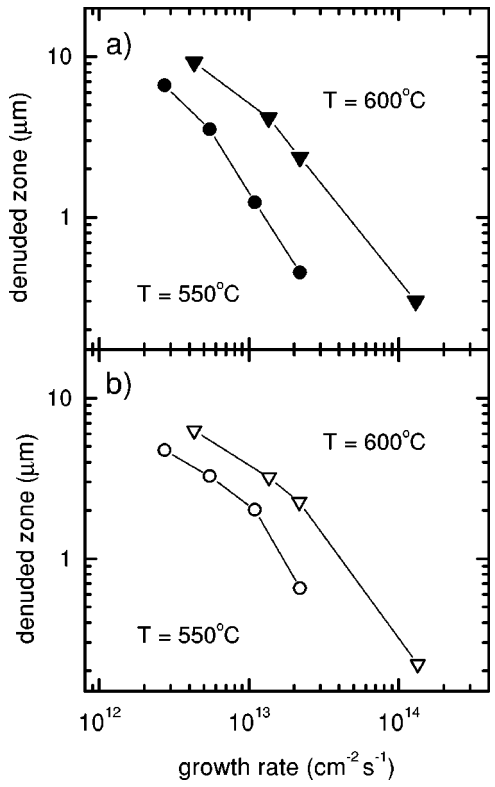

FIG. 9. Width of the denuded zone w as a function of growth rate for 550 °C and 600 °C from (a) experiment and (b) the 1D model of section IV. The growth rate is given in units of the flux of Ge atoms.

ent in the region $x \approx x_0$, the wetting layer grows more rapidly near $x=0$ and depletes the wetting layer in the surrounding areas, $1.5<x<4$ μm. Near $x=0$, the wetting-layer thickness surpassed $h=4a$ after deposition of only ≈ 2 eq ML, islands have nucleated, and therefore the wetting layer thickness is reduced to $h \approx 3a$. With continued deposition, see Figs. 8(b) and 8(c), new islands nucleate only in the region $x>3.5$ μm, leaving a ≈ 3 μm wide region that is completely free of islands.

V. DISCUSSION

The one-dimensional model described in Sec. IV successfully reproduces all of the important behavior seen in the experiments. A summary is given in Fig. 9. For the experimental data, we define the width of the denuded zone w as the distance between the edge of the laser dimple and the point at which the island density falls by a factor of 1/2 relative to the island density far from the dimple. In the 1D model, the spatial dependence of the island densities is difficult to measure with good statistics; therefore, we define w as the width of the region that is completely free of islands.

At low growth rates F, the calculations approach the scaling $w \propto F^{-1/2}$ expected if w is controlled by diffusive transport during a time scale $\Delta t \propto 1/F$. In fact, using $\Delta t = 2(\sigma F)^{-1}$ (the time difference between nucleation on the dimple and nucleation on the surfaces far from the dimple) gives a diffusion length $L_d = \sqrt{8Dn_0/F} \approx 5$ μm for $Dn_0 = 1.5\times 10^5\ s^{-1}$ and $F = 5\times 10^{12}\ cm^{-2}\ s^{-1}$. Thus, at least at low growth rates, the width of the denuded zone is determined by the diffusion length, $w \approx L_d$, with Δt controlled by the time of early nucleation on the dimple. At high growth rates, w falls off more quickly than $F^{-1/2}$ because the chemical-potential gradient created by the dimple morphology becomes less effective in depleting the wetting layer in the surrounding region; i.e., the time difference between nucleation on the dimple rim and nucleation on the surfaces far from the dimple decreases rapidly with increasing F.

Unfortunately, we cannot determine the prefactor ν and the activation energy (E_m+E_f) of Eq. (7) independently because the useful temperature range for our experiments is limited. At $T \leqslant 500$ °C a measurable denuded zone exists only for very low growth rates, on the order of monolayers per hour, where possible contamination from the background pressures of water vapor, CO and hydrocarbons creates uncertainty in the reliability of the data. Surprisingly, the denuded zone is also absent for growth at $T \geqslant 700$ °C (data not shown); intermixing of the Ge wetting layer with the Si substrate becomes pronounced at these temperatures and, apparently, this alloying disrupts the driving force for early nucleation on the rim of the laser dimples.

VI. CONCLUSIONS

Our simple one-dimensional model of mass transport and island nucleation captures the essential physics of how the denuded zone varies with flux and temperature. While the model has many parameters, the results are sensitive to only the transport rate Dn_0 and the size of the region x_0 that models the chemical potential gradient created by the morphology of the laser dimple. By adjusting these two parameters to fit eight experiments at 550 °C and 600 °C, we determine $Dn_0 \approx 1.5\times 10^5\ s^{-1}$ at 600 °C. Assuming that the transport rate is thermally activated, $Dn_0 = \nu \exp(-E/k_BT)$ with $\nu = 5\times 10^{12}\ s^{-1}$, the activation energy of the transport rate is $E = E_m + E_f = 1.3$ eV.

Our experimental approach—manipulation of island densities through subtle changes in substrate morphology—should be generally applicable to other S-K growth systems as long as the chemical potential of the wetting-layer depends on surface orientation. Quantitative measurements of the wetting layer transport rate Dn_0 will provide needed constraints on theory and facilitate the design of experiments directed at understanding and controlling the growth of epitaxial nanostructures using the Stranski-Krastanov growth mode.

ACKNOWLEDGMENTS

This work was supported by National Science Foundation Grant No. DMR-9705440 and the U.S. Department of Energy, Division of Materials Sciences, under Award No. DEFG02-91ER45439. Sample characterizations by AFM, SEM, and RBS took place at the facilities of the Center for Microanalysis of Materials at the University of Illinois.

[1] D. J. Eaglesham and M. Cerullo, Phys. Rev. Lett. **64**, 1943 (1990).
[2] T. I. Kamins, G. Medeiros-Ribeiro, D. A. A. Ohlberg, and R. S. Williams, J. Appl. Phys. **85**, 1159 (1999).
[3] F. M. Ross, J. Tersoff, and R. M. Tromp, Phys. Rev. Lett. **80**, 984 (1998).
[4] J. S. Sullivan, H. Evans, D. E. Savage, M. R. Wilson, and M. G. Lagally, J. Electron. Mater. **28**, 426 (1999).
[5] I. Daruka, J. Tersoff, and A.-L. Barabási, Phys. Rev. Lett. **82**, 2753 (1999).
[6] C.-P. Liu, J. M. Gibson, D. G. Cahill, T. I. Kamins, D. P. Basile, and R. S. Williams, Phys. Rev. Lett. **84**, 1958 (2000).
[7] T. I. Kamins, R. S. Williams, and D. P. Basile, Nanotechnology **10**, 110 (1999).
[8] T. I. Kamins, D. A. A. Ohlberg, R. S. Williams, W. Zhang, and S. Y. Chou, Appl. Phys. Lett. **74**, 1773 (1999).
[9] E. S. Kim, N. Usami, and Y. Shiraki, Appl. Phys. Lett. **72**, 1617 (1998).
[10] M. Krishnamurthy, B.-K. Yang, J. D. Weil, and C. G. Slough, Appl. Phys. Lett. **70**, 49 (1998).
[11] T. Ishikawa, S. Kohmoto, and K. Asakawa, Appl. Phys. Lett. **73**, 1712 (1998).
[12] K. Brunner, J. Zhu, C. Miesner, G. Abstreiter, O. Kienzle, and F. Ernst, Physica E (Amsterdam) **7**, 881 (2000).
[13] G. Jin, J. L. Liu, S. G. Thomas, Y. H. Luo, K. L. Wang, and B.-Y. Nguyen, Appl. Phys. A: Mater. Sci. Process. **70**, 551 (2000).
[14] J. A. Venables, Philos. Mag. **27**, 697 (1973).
[15] R. M. Tromp and M. Mankos, Phys. Rev. Lett. **81**, 1050 (1998).
[16] T. I. Kamins, G. Medeiros-Ribeiro, D. A. A. Ohlberg, and R. S. Williams, Appl. Phys. A: Mater. Sci. Process. **67**, 727 (1998).
[17] G. Medeiros-Ribeiro, T. I. Kamins, D. A. A. Ohlberg, and R. S. Williams, Phys. Rev. B **58**, 3533 (1998).
[18] S. A. Chaparro, Y. Zhang, J. Drucker, D. Chandrasekhar, and D. J. Smith, J. Appl. Phys. **87**, 2245 (2000).
[19] T. I. Kamins, E. C. Carr, R. S. Williams, and S. J. Rosner, J. Appl. Phys. **81**, 211 (1997).
[20] M. Krishnamurthy, J. S. Drucker, and J. A. Venables, J. Appl. Phys. **69**, 6461 (1991).
[21] T. Schwarz-Selinger, D. G. Cahill, S.-C. Chen, S.-J. Moon, and C. P. Grigoropoulos, Phys. Rev. B **64**, 155 323 (2001).
[22] N. C. Bartelt and R. M. Tromp, Phys. Rev. B **54**, 11 731 (1996).
[23] Q. Lu, T. R. Bramblett, N. Lee, M. Hasan, T. Karasawa, and J. E. Greene, J. Appl. Phys. **77**, 3067 (1995).
[24] H. Kim, N. Taylor, T. R. Bramblett, and J. E. Greene, J. Appl. Phys. **84**, 6372 (1998).
[25] H. Kim, N. Taylor, J. R. Abelson, and J. E. Greene, J. Appl. Phys. **82**, 6062 (1998).
[26] H. Kim and J. E. Greene, J. Vac. Sci. Technol. A **17**, 354 (1999).
[27] M. Mayer, computer code SIMNRA, User's Guide IPP Report No. 9/113 (Max-Planck-Institut für Plasmaphysik, Garshing, Germany, 1997).
[28] J. F. Ziegler, J. P. Biersack, and U. Littmark, *The Stopping and Ranges of Ions in Matter* (Pergamon Press, New York, 1985), Vol. 1.
[29] J. Tersoff, Phys. Rev. B **43**, 9377 (1991).
[30] I. Daruka and A.-L. Barabási, Appl. Phys. Lett. **72**, 2102 (1998).
[31] V. Le Thanh, V. Yam, Y. Zheng, and D. Bouchier, Thin Solid Films **380**, 2 (2000).
[32] A. Vailionis, B. Cho, G. Glass, P. Desjardins, D. G. Cahill, and J. E. Greene, Phys. Rev. Lett. **85**, 3672 (2000).